Postprint of: de Freitas Araújo K. C., Vieira dos Santos E., Pierpaoli M., Ficek M., Santos J. E. L., Martínez-Huitle C. A., Bogdanowicz R., Diamondized carbon nanoarchitectures as electrocatalytic material for sulfate-based oxidizing species electrogeneration, ELECTROCHIMICA ACTA, Vol. 430 (2022), 141069, DOI: 10.1016/j.electacta.2022.141069

Diamondized carbon nanoarchitectures as electrocatalytic material for sulfate-based oxidizing species electrogeneration

Karla Caroline de Freitas Araújo[1], Elisama Vieira dos Santos[1], Mattia Pierpaoli[2], Mateusz Ficek[2], José Eudes L. Santos[1], Carlos A. Martínez-Huitle[1,*] Robert Bogdanowicz[2,*]

[1]*Instituto de Química, Universidade Federal do Rio Grande do Norte, Natal, Rio Grande do Norte, Brazil.*

[2]*Faculty of Electronics, Telecommunications and Informatics, Gdańsk University of Technology, 11/12 G. Narutowicza St, 80-233 Gdańsk, Poland*

*Corresponding author's e-mail:

carlosmh@quimica.ufrn.br (C.A. Martínez-Huitle),

rbogdan@eti.pg,edu.pl (Robert Bogdanowicz)

Abstract

The introduction of nanotechnology seems to be an imperative factor to intensify the synergic effects of electrocatalytic materials to produce strong oxidant species or to increase the active sites on their surfaces as well as to enhance the conversion yield in a fuel cell, high-added value products, electrolytic treatment for environmental protection or the detection limit in electroanalysis. Recently, a new type of 3D-diamond electrodes was developed with boron-doped carbon nanowalls (B:CNW), which was manufactured using the microwave plasma-assisted chemical vapor deposition (CVD) process, improving the charge transfer and enhancing the electrochemical performance. The applicability of a BDD/boron-doped carbon nanowalls (BDD/B:CNW) anodes to degrade organic pollutants has been already investigated; however, no attempts at the electrosynthesis of oxidizing species using these diamond-carbon nanostructures have been reported yet. Therefore, the electrosynthesis of sulfate-based oxidizing species was studied here to answer relevant questions from both fundamental and practical point-of-view. The results demonstrated that persulfate was efficiently produced at the BBD plate, while that the ion-radical sulfate could be the most important oxidant at BDD/B:CNW anode when compared to other electrocatalytic materials, including BDD surfaces. Persulfate concentrations ranged from 3 to 6 μM, depending on the applied current density (2.5, 5.0, and 15 mA cm^{-2}), at diamond electrodes. A dye-model pollutant - methyl orange (MO) was degraded below the limit of detection within 45 min using BDD/B:CNW when *in-situ* sulfate-based oxidizing species were electrogenerated. These kinds of 3D-diamond-carbon nanostructures are thus promising as novel electrocatalyst for various catalytic applications in the environmental and energy fields.

Keywords: boron-doped diamond electrode, sulfate-based oxidizing species, diamond-carbon nanoarchitectures, electrocatalyst, electrogeneration.

1. Introduction

The scientific community has shown a preference to apply EO as an environment-friendly electrochemical process because of its uncomplicatedness and acceptance among the electrochemical advanced oxidation processes (EAOPs), in terms of electrolytic technology, amenability, environmental compatibility, automation, no reagents use, renewable energies-driven and in-situ production of higher concentration of oxidants [1]. In the last decades, EO has competently demonstrated its effectiveness to mineralize different organic compounds in a great variety of water matrices or wastewaters [2]. Nevertheless, the extension of mineralization/degradation of these pollutants and their concentration as well as the type of the electrogenerated oxidants strongly depends on the operating parameters and the nature of the anode electrocatalytic material [3,4].

Various electrodes have been used in EO, like Ir-, Pt-, Ru-, Ti-, Pb- and Sn- oxide-based anodes as well as synthetic diamond films [5,6]. However, boron-doped diamond (BDD) anodes are considered the most effective electrocatalytic materials for degrading/mineralizing refractory/priority pollutants and waterborne agents [1,2,7–9]. It is due to their effective *in-situ* production of oxidizing agents, at higher concentrations, mainly reactive oxygen species (ROS) (Eq. (1)-(5)) [9]. Also, peroxodisulfate ($S_2O_8^{2-}$), peroxodicarbonate ($C_2O_6^{2-}$) and peroxodiphosphate ($P_2O_8^{4-}$) can be electrochemically formed with ROS from the oxidation of sulfate or bisulfate by Eq. (6), bicarbonate by Eq. (7) and phosphate by Eq. (8) at the BDD surface [10,11].

$$BDD + H_2O \rightarrow BDD(^{\bullet}OH) + H^+ + e^- \quad (1)$$

$$^{\bullet}OH \rightarrow {}^{\bullet}O + H^+ + e^- \quad (2)$$

$$2\,{}^{\bullet}O \rightarrow O_2 \quad (3)$$

$$2^{\bullet}OH \rightarrow H_2O_2 \quad (4)$$

$$O_2 + {}^{\bullet}O \rightarrow O_3 \quad (5)$$

$$2SO_4^{2-} \rightarrow 2SO_4^{-\bullet} \rightarrow S_2O_8^{2-} + 2e^- \quad (6)$$

$$2HCO_3^- \rightarrow C_2O_6^{2-} + 2H^+ + 2e^- \quad (7)$$

$$2PO_4^{3-} \rightarrow P_2O_8^{4-} + 2e^- \quad (8)$$

As already scientifically stated, the effective electrosynthesis of oxidizing species requires an electrode with a large surface area, high electrocatalytic activities, long-term stability, as well as a low cost of materials [5,12]. Thus, the introduction of nanoarchitectures seems to be an essential factor to intensify the synergic effects of electrocatalytic materials to produce strong oxidant species or to increase the active sites on their surfaces [13]. Novel nanostructured materials can exhibit better electrochemical properties than their bulk counterparts with a specific pore dimension distribution and well-defined structure-morphology, maximizing the exposed-surface area and minimizing the mass transport phenomena [14–16]. Thus, the advances in the preparation of highly sophisticated electrocatalytic nanomaterials may lead to further improvements in the mineralization of organic pollutants as well as the electrosynthesis of oxidants, making them suitable for smart water solutions [17]. These technologies will play a key role in achieving the Sustainable Development Goal 6 (SDG6) since these represent a substantial opportunity if their implementation is carried out to guarantee sustainability and increase competence in water management (to treat and distribute water for human use) [18].

Recently, a versatile electrode was discovered, called the "3D-nanostructured BDD/B:CNW" anode. This 3D-diamondized-carbon nanostructure possesses extraordinary electrochemical properties (e.g., peculiar morphology, specific surface area and the larger extends of exposed

edges with a greater number of functional groups and chemisorbed heteroatoms, in particular, oxygen), allowing a higher reactivity of the carbonaceous nanostructure for environmental, fuel and sensors applications, compared to 2D-BDD electrode [19–21]. However, no information concerning the effectiveness of this 3D-nanostructured BDD/B:CNW anode to electrogeneration oxidants has been reported yet. Thus, for the first time, the electrosynthesis of sulfate-based oxidants species has been studied by using a 3D-nanoarchitectured BDD/B:CNW anode to answer relevant questions from both fundamental and practical point-of-view. An organic model compound was also chosen to prove the oxidative efficiency of *in-situ* $S_2O_8^{2-}$ electrogeneration when compared with other electrode materials. The results are discussed considering the existing literature on nanostructured electrodes for electrocatalytic advanced oxidation processes.

2. Materials and Methods

2.1. Materials

All reagents were of analytical grade and used without further purification. The water was obtained from purified water (Milli-Q system, with resistivity ≥18 MΩ cm at 25 °C). Methyl orange (MO) purity was 95% and it was used as received.

2.2. Synthesis and characterization of BDD/B:CNW

BDD and BDD/BCNW were synthesized using the MWPECVD system (SEKI Technotron AX5400S, Japan). Thin films were grown on niobium substrates for a total of 5 h, resulting in 3 µm of thickness. The detailed parameters of the thin film synthesis can be found elsewhere, for BDD [ref1] and for the BDD:BCNW in Pierpaoli et al [ref2, ref3]~~BCNW in Siuzdak *et al.* [22], Dettlaff *et al.* [23], and Sobaszek *et al.* [24]~~ . The surface characteristics

of the BDD/B:CNW was carried out using a Hitachi model TM 3000 top microscope with a high sensitivity semiconductor backscattered electron detector to obtain scanning electron microscopy (SEM) images, using a significant magnification and operating at 15 kV voltage acceleration with a tungsten filament. The SEM images were taken under a vacuum at controlled temperatures and the energy dispersive X-ray (EDS) spectrum was obtained to analyze the concentrations of the elements in the diamond-carbon nanostructures. Raman spectra were recorded in the 50–3200 cm^{-1} range, upon excitation by a 532 nm laser; the spectral resolution was equal to 2.9 cm^{-1}, in the range of 50–2000 cm^{-1} and 2.4 cm^{-1} in the range of 2000–3200 cm^{-1} with an integration time of 5 s (20 averages), with a diffraction grating of 300 lines/mm^2.

2.3. Electrochemical measurements

Experiments were carried out in a conventional three-electrode system in Pyrex material with a capacity of 10 mL, and measurements were performed between 0.0 and +1.8 V at 10 mV s^{-1} for quasi-steady polarization curves in 0.05 M of Na_2SO_4. BDD and BDD/B:CNW anodes have significant areas in cm^2, however, an exposed geometric area of ca. 0.075 cm^2 was used as the working electrode for electrochemical measurements, while this area was increased for bulk electrolysis (see next subsection). A platinum wire and an Ag/AgCl (3 M) were employed as the auxiliary and reference electrodes, respectively. The electroactive surface area (A_{real}) and the differential capacitance (C_{DL}) were experimentally estimated [25–27], according to Eq. 1. To do that, a potential range was selected, for BDD and BDD/B:CNW electrodes, where a non-Faradaic current response is registered. This range was ≈0.2 V potential window centered on the open-circuit potential of the system. Then, cyclic voltammetry (CV) measurements were conducted in static solution by sweeping the potential

across the non-Faradaic region and back at 9 different scan rates (0.02, 0.04, 0.06, 0.08, 0.10, 0.12, 0.14, 0.16, 0.18 and 0.20 V s^{-1}) at 25±1°C in 0.05 M of Na_2SO_4. For each measurement, five voltammetric profiles were recorded, and the last curve was always selected to be used for plotting the graphics in this work.

$$A_{real} = \frac{C_{DL}}{C^*} = \frac{\mu F}{\frac{\mu F}{real\ cm^2}} = cm^2 \quad (1)$$

In Eq. 1, C_{DL} is the differential capacitance of the electrode-electrolyte interface and C* is approximately 60 μF (real cm^2)$^{-1}$ which is a reference value for porous materials, regardless of its composition [25,27]. Experiments were performed with an Autolab potentiostat/galvanostat model PGSTAT302N.

2.4. Spectrophotometric analysis

For UV-vis spectrophotometric measurements to determine the production of persulfate, a Shimadzu spectrophotometer model 1800 was employed by using *in-situ* chemical oxidation (ISCO) method [28,29], operating from 190 to 800 nm. A single quartz cuvette was used with an optical path of 1 cm. It is important to remark that persulfate generation can be followed by ISCO method without H_2O_2 interference because the analysis of absorption spectra of a yellow color solution resulting from the reaction of persulfate and iodide in the presence of sodium bicarbonate reveals a clear absorbance spectrum at 352 nm.

2.5. Electrochemical determination of methyl orange concentration

Electroanalytical measurements were carried out in a conventional three-electrode system in Pyrex material with a capacity of 25 mL for determining MO concentrations by differential pulse voltammetry (DPV) analysis. BDD anode (silicon substrate, 500 ppm of boron doping,

2-3 μm of thickness), with an exposed geometric area of 0.28 cm^2, was used as the working electrode, while a platinum wire and Ag/AgCl (KCl 3 M) were employed as the auxiliary and reference electrodes, respectively. DPV experiments were performed with an Autolab PGSTAT 320N model to establish an analytical curve by measuring different concentrations of MO in 0.05 M Na_2SO_4. Other details of the procedure are as follows: equilibration time, 5 s; modulation time, 0.05 s; interval time, 0.5 s; initial potential, 0 V; end potential, +1.8 V; step potential, 25 mV; and modulation amplitude, 100 mV. For determining MO concentration at each predetermined time during EO tests, the samples were spiked with a known quantity of a standard solution, and the standard addition method was implemented.

2.6. Bulk experiments

Experiments were carried out using a bulk electrochemical cell under stirring agitation which consisted of several electrodes (anodes such as BDD plate, BDD/B:CNW, TiPt, Pb/PbO_2, Ti/TiO_2-nanotubes/PbO_2 and Ti as cathode, respectively) of 1.5 cm of diameter (geometrical area ≈7.07 cm^2). Electrolysis of 50 mL of a synthetic solution containing 0.05 M Na_2SO_4 as the supporting electrolyte was performed by applying 2.5, 10, and 15 mA cm^{-2} for 150 min to prepare sulfate-based oxidizing species. Sulfate concentration was chosen based on the existing literature to produce a significant concentration of persulfate [29,30]. During all experiments, samples of the sulfate-based oxidizing solutions were collected at the end of the electrolysis, and subsequently, these were analyzed by the ISCO-spectrophotometric method, determining the final sulfate-based oxidants concentration produced. For the EO of an organic target compound, 25 mL of 0.05 M of Na_2SO_4 containing 10 mg L^{-1} of MO were electrochemically treated by mixing with magnetic stirring for 40 min and aliquots were

withdrawn at predetermined times to determine chemical oxygen demand (COD) and the concentration of the target pollutant by the electroanalytic procedure. COD levels were measured by using pre-dosed reagents (HANNA® vials) in 2 mL samples. Samples for COD determination were digested in a thermal reactor (HANNA instrument) at 150°C for 2 h. Subsequently, the samples initial and final, for all oxidation tests, were analyzed on a spectrophotometer (Hanna HI 83099), at 25°C.

3. Results and Discussion

3.1. Characterization of diamond electrode

The BDD/B:CNW electrode morphology presents microscale valleys with a diameter of a few micrometers, as observed in the SEM images (Fig. 1a). As previously reported [13,14,31] and confirmed by SEM images; on the one hand, carbon grows vertically in form of multi-layer graphene walls covered by diamond clusters. Microcavities having an opening in the range between tens and hundreds of nanometres are formed between the nanowall boundaries (Fig. 1a). On the other hand, "nano-flaps" also grow perpendicularly as secondary protuberances to the surface of the nanowalls due to the process of synthesis [13,14,31]. Meanwhile, EDS spectrum evidence that the concentrations of the elements in the diamond-carbon nanostructures are preferentially carbon and oxygen, confirming the BDD/B:CNW composition (Fig. 1b).

In this context, the CVD process developed by Bogdanowicz's group [14] is an innovative approach to obtaining a carbon nanostructure with concave and convex curvatures in a simple way [13,14,31]. Thus, it was possible to understand that the electrode surface and their composition, as well as the density of electronic states of electrode materials [XXX], could influence during the production of oxidant species. From the Raman spectra (Fig. 1c), the

intense peak at 1332 cm−1 sharply observed for the BDD sample is assigned to sp3-hybridized carbon, which decreases in intensity and downshift to 1310 cm-1 for the BDD:BCNW sample, which is typical for typical for heavily boron-doped diamond [ref], since the diborance concentration inside the reactor increases as well. Moreover, it is possible to observe the G-band at around 1580 cm−1, arising from the presence of graphitic material (i.e., sp2-C), and the D-band which indicates defects in graphitic structures. Finally, D' is another second-order Raman band, appearing as a shoulder peak of the G band, originating from a second-order Raman scattering at the K point, involving one iTO phonon and one defect state [ref].

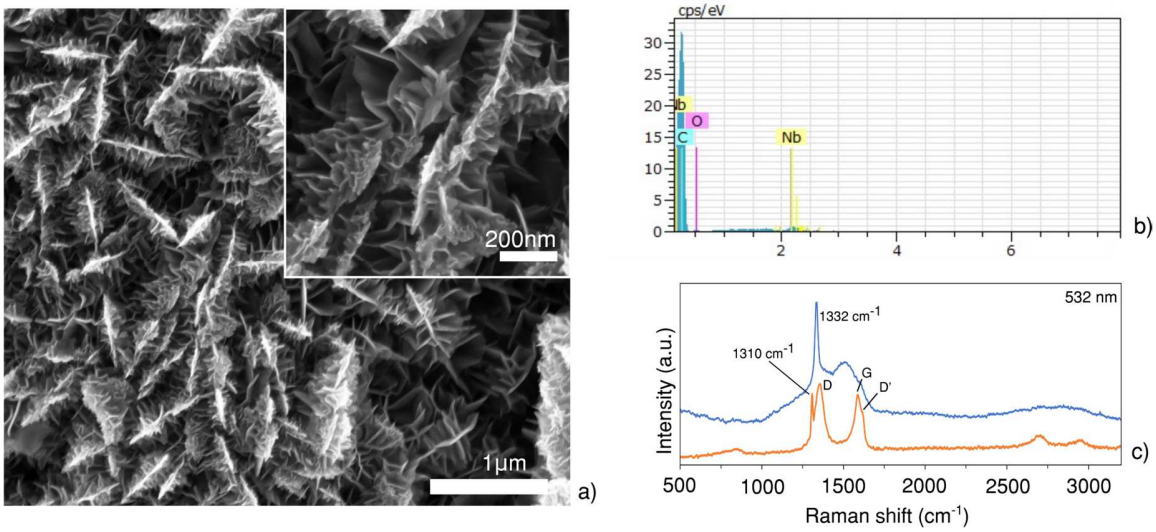

Fig. 1. (a) SEM images of the BDD/BCNW grown on Nb, (b) EDS spectrum, confirming the composition of BDD/BCNW electrode: C (94.42 wt.%, 97.40 at.%), O (2.90 wt.%, 2.25 at.%) and Nb (2.68 wt.%, 0.36 at.%). And (c) Raman spectra for the BDD and BDD:BCNW samples.

3.2. Electrochemical measurements

CV curves in a non-faradaic potential range were recorded at different scan rates (0.04, 0.06, 0.08, 0.10, 0.12, 0.14, 0.16, 0.18 and 0.20 V s^{-1}) to estimate the electro-active surface of BDD and BDD/B:CNW electrodes. By plotting the current, which was measured in the middle of the double-layer region and recorded at different scan rates, versus the scan rate (e.g.: BDD/B:CNW, Fig. 2); a straight line was obtained, which allowed determining the double layer capacitance values for these electrocatalytic materials (Insets in Fig. 2). Then, by using the Eq. (1), the geometric area of the electrodes (≈0.075 cm^2) and the C_{DL} values obtained (5.40 µF and 41.52 µF for BDD and BDD/B:CNW, respectively); the real surface areas were estimated, obtaining 0.216 cm^2 and 0.692 cm^2 for BDD and BDD/B:CNW, respectively. It is important to remark that, based on existing literature data [26], reference values (C*) for compact and porous materials should be considered to estimate the electroactive surface area, regardless of its composition. Then, 60 µF (real cm^2)$^{-1}$ was the reference value for BDD/B:CNW, while, 25 µF (real cm^2)$^{-1}$ for BDD plate due to the most homogeneous surface [26,27,32].

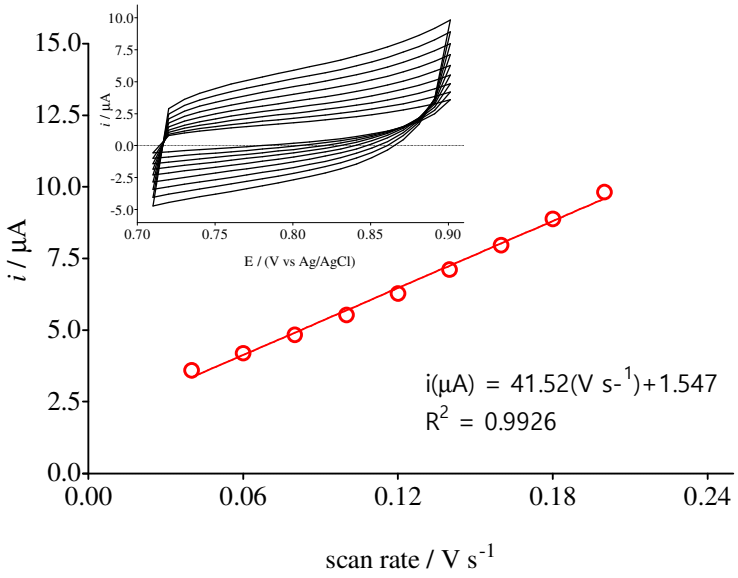

Fig. 2. Cyclic voltammetric (CV) analysis (from 0.04 to 0.20 V s^{-1}) to estimate the capacitance for BDD/B:CNW electrode in 0.05 M of Na_2SO_4 by plotting the current values in the double-layer regions as a function of scan rate. Inset: double-layer capacitance measurements by using CV technique at different scan rates.

Although there are several methods to experimentally determine the real surface area such as hydrogen adsorption, double layer capacitance, surface oxide reduction, underpotential deposition of metals, and adsorbed carbon monoxide stripping [27]; for the case of BDD electrodes, some approaches could be efficiently applied. However, the double-layer capacitance method allows to obtain accurate surface measurements, avoiding significant surface changes due to the oxygen/hydrogen evolution, formation/reduction of oxides, and modification of carbon materials [27,32,33]. The double-layer capacitance also allows measuring the total surface area accessible to the solution, and it is not destructive [27]. In fact, in this case, the real electrode areas are superior to the geometrical value; it could be due to the character of diamond surfaces, allowing for proper contact of the solution with all active sites and consequently, a significant increase in the real area was achieved respect to 0.075 cm^2.

For BDD/B:CNW electrode, an increase in the porous properties of the material was achieved due to the 3D nanostructures (see SEM images, Fig. 1) [20,21,24]; for this reason, an increase in the solution contact (solution diffusion between/into the porous) could be expected [14]. Meanwhile, this behavior is reduced in the BDD plate due to the homogeneous surface. In this context, the roughness factor ($RF = A_{real}/A_{geometric}$) was also determined for BDD and

BDD/B:CNW electrodes, considering the geometric surface and the estimated electroactive area for each one of the electrodes, achieving values of about 2.88 and 9.22, respectively. From these results, it is possible to deduce that, the new type of 3D-diamond electrodes with boron-doped carbon nanowalls (B:CNW) increased its roughness by about 3.2-folds in comparison to the BDD plate surface [14,15,21,34,35]. This result evidenced that, the roughness controls the contact of the active sites with the solution and thus, increasing its active area [14,21].

On the other hand, it is important to characterize the potential window and anodic oxygen evolution reaction by electrochemical measurements at both carbon materials. Fig. 3 shows the polarization curves registered at BDD and BDD/B:CNW anodes in a sulfate solution. A slight variation in the potential window is achieved, evidencing an important change in the potential of the oxygen evolution reaction (OER). This behavior is mainly associated with the different carbon constituents on the BDD surfaces as well as the electrochemical decomposition of the supporting electrolyte [30,36,37]. Linear polarization curves for BDD/B:CNW electrode showed that the potential for the OER was shifted to a less positive potential (≈1.43 V vs Ag/AgCl). Based on previous works [36,38], it was demonstrated that graphite electrode presents lower oxygen overpotential than BDD electrodes, similar to the behavior achieved at BDD/B:CNW. Conversely, BDD plate showed to be a poor electrocatalyst for OER, shifting this reaction to more positive potentials (Fig. 3).

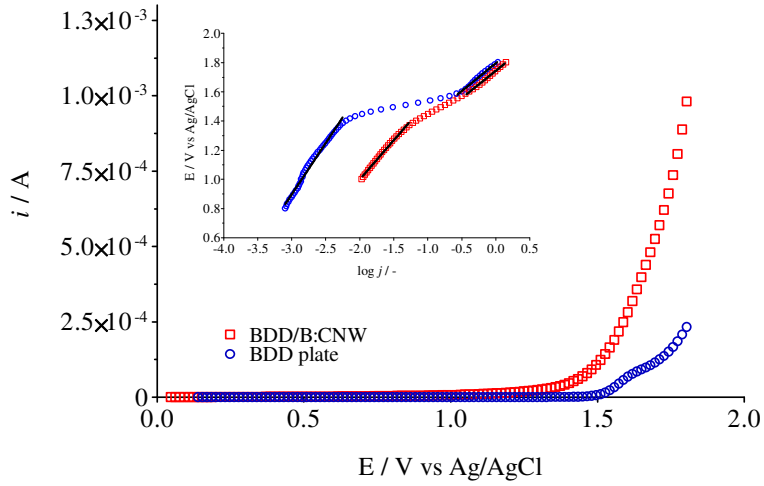

288

289 **Fig. 3.** Polarization curves registered at BDD and BDD/B:CNW electrodes in 0.05 M of
290 Na_2SO_4. Inset: data in terms of Tafel plots at lower and higher overpotential regions from the
291 potential of hydroxyl radicals' formation.

292

293 Meanwhile, additional effects could be observed when the analysis of the Tafel plots
294 is executed. E/log *j* plots at both BDD electrodes are shown in the inset of Fig. 3, considering
295 the real surface area for each one of them. As can be observed, the Tafel plots change their
296 slope according to the lower overpotential region (<1.6 V) or high overpotential region
297 (>1.62 V). At BDD/B:CNW, the OER seems to be the main process than that registered at
298 BDD plate. However, no unique slope can be attributed to the Tafel plots at both BDD
299 electrodes due to the complex set of the electrochemical reactions taking place involving
300 most probably the OER and persulfate production. Tafel slopes about 0.6117 V decade^{-1} and
301 0.5363 V decade^{-1} for BDD plate and BDD/B:CNW electrode were estimated, respectively,
302 at lower overpotential region. Meanwhile, 0.3810 V decade^{-1} and 0.3740 V decade^{-1} in the

high overpotential region were obtained for BDD plate and BDD/B:CNW electrodes, respectively. Two distinct linearity regions can be attributed to the electrochemical reactions on the Nernst layer at BDD surface, associated with the sulfate ions in solution and water discharge, which are transformed to persulfate and hydroxyl radicals (•OH) as well as oxygen, respectively [39,40]. From Tafel plots data as well as the current and potentials (inset of Fig. 3), it is possible to infer that an important electrochemical reaction at the lower overpotential region is attained at both diamond electrodes, which could be associated with the specific interaction of sulfate ions with each one of the carbon surfaces [37,40,41].

Based on the existing literature [3,4,8], in the case of diamond electrodes, the mechanisms followed depend strongly on (i) extension of the oxidation of SO_4^{2-} ions at the diamond surface, via direct electron transfer, to produce persulfate (Eq. 2), (ii) the production of •OH at anode surface in the reaction cage (Eq. 1), (iii) the interaction of •OH with SO_4^{2-} ions, in the Nernst layer, to favor the production of $SO_4^{-\bullet}$ (principal intermediate) and subsequently, persulfate (Eq. 3), as well as, in some cases, the association between the sp^2-impurities on its surface and the adsorption of SO_4^{2-} ions on these active sites to also form $SO_4^{-\bullet}$ and then, producing persulfate (Eqs. 4 and 5),

$$2SO_4^{2-} \rightarrow S_2O_8^{2-} + 2e^- \quad (2)$$

$$SO_4^{2-} + {}^{\bullet}OH \rightarrow SO_4^{-\bullet} + H^+ + e^- \quad (3)$$

$$BDD(SO_4^{2-}) \rightarrow BDD(SO_4^{-\bullet}) + e^- \quad (4)$$

$$BDD(SO_4^{-\bullet}) + SO_4^{-\bullet} \rightarrow S_2O_8^{2-} \quad (5)$$

In the case of the BDD plate, the electrochemical reactions, which occurs at the lower overpotential region (<1.6 V), a more strong interaction is attained than that at BDD/B:CNW.

The Tafel slope is higher than the other one (0.6117 V decade^{-1} and 0.5363 V decade^{-1}, for plate BDD and BDD/B:CNW electrode, respectively). These behaviors appear to be associated to the production of $S_2O_8^{2-}$ or $SO_4^{-\bullet}$ at BDD surface [41], evidencing that, a direct electron transfer is attained at BDD plate, in the former. While a fast-adsorptive interaction of SO_4^{2-} ions on B:CNW-active sites (sp^2-configuration) is achieved to form $SO_4^{\bullet-}$ at BDD/B:CNW electrode (Eq. 8) [36]. Afterward, at both electrodes, similar surface-layer-based approaches are accomplished at a higher overpotential region (>1.6 V), which are related to the production of $^{\bullet}OH$ (Eq. 1) and O_2 (Eq. 6) as well as the formation of sulfate-based oxidizing species (such as $SO_4^{-\bullet}$ (Eq. 3) or $S_2O_8^{2-}$ (Eq. 3 and 7)) by the participation of free heterogeneous $^{\bullet}OH$ (Eq. 3).

$$2^{\bullet}OH \rightarrow O_2 + 2H^+ + 2e^- \quad (6)$$

$$SO_4^{-\bullet} + SO_4^{2-} \rightarrow S_2O_8^{2-} + e^- \quad (7)$$

It is important to remark that, the surface-layer-based processes are achieved closer to the electrode surface, in the Nernst layer (from Armstrong to nanometers), which mainly depend on the diffusion distance of the free heterogeneous $^{\bullet}OH$, the thickness of the diffusion layer, the convection (agitation and flow rate) and the diffusion coefficient of SO_4^{2-} ions in the solution [8]. However, the limiting steps to produce $S_2O_8^{2-}$ could be regarded as the diffusion of sulfate in the diffusion layer to react with the free heterogeneous $^{\bullet}OH$ (Eq. 3) as well as the subsequent reactions at BDD ($SO_4^{-\bullet}$)-sites on diamond surface (Eq. 5).

For this reason, it is necessary to control the current density to stabilize the $S_2O_8^{2-}$ electrogenerated, determining the extension of the production of $S_2O_8^{2-}$ at both electrodes.

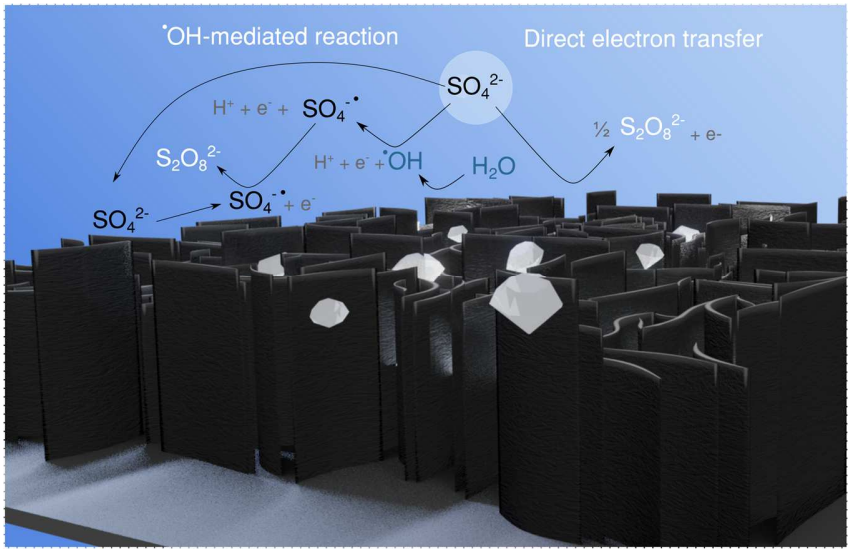

Fig xx – Schematic representation of the persulfate reaction pathway on the BDD/BCNW electrode

3.3. Electrochemical production of persulfate

By applying different current densities (2.5, 5.0 and 15.0 mA cm^{-2}) at 25 °C, the $S_2O_8^{2-}$ concentration produced at both electrodes was determined by ISCO method (Fig. 4). Based on the existing literature, the maximum $S_2O_8^{2-}$ concentration is achieved between 120 and 150 min of electrolysis (inset in Fig. 4), then, the final persulfate concentration was plotted for all electrocatalytic materials at different applied current densities (Figure 4).

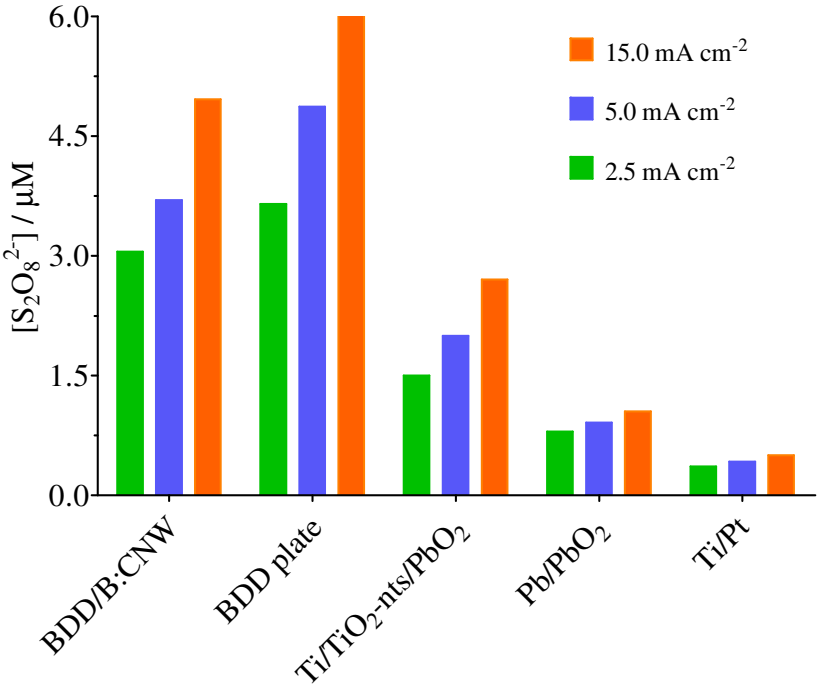

356

357 **Fig. 4.** Electrochemically persulfate generated at different anode materials. Batch cell with
358 50 mL of 0.05 M Na_2SO_4 at 25°C.

359 As can be observed, an increase in the concentration of persulfate was attained when
360 the applied current density was increased (Fig. 4). For BDD plate, a significant enhancement
361 in the production of persulfate was attained concerning those achieved at BDD/B:CNW
362 electrode. This behavior is related to the favored mechanism to electrogenerated persulfate
363 [8]. According to the Tafel plot analysis, a stronger interaction is attained at a lower
364 overpotential region (<1.6 V) which indicated that the electrochemical production of $S_2O_8^{2-}$
365 via direct electron transfer could be attained at BDD plate [3,8]. Meanwhile, at higher
366 potentials, the production of $^{\bullet}OH$ radicals favors an enhancement of the persulfate
367 concentration [29]. Conversely, at BDD/B:CNW anode, the production of persulfate depends

on the formation of $SO_4^{-\bullet}$ at BDD surface (which seems to be the main intermediate), and the subsequent surface-layer-based reactions of $SO_4^{-\bullet}$ [10,37,42,42]. In this sense, the results related to the quantification of persulfate concentration indicated that the extension of the persulfate mechanism depends on the nature of the electrode and the *j* (which is directly associated with the cell potential). In fact, at lower *j*, the increase in the persulfate concentration is less significant than those achieved when higher *j*. For example, at BDD plate, from 2.5 to 5.0 mA cm^{-2}, the persulfate concentration increases by 1.33-folds, while from 5.0 to 15.0 mA cm^{-2}, it increases by 1.64-folds. Similar behavior is observed at BDD/B:CNW anode, where increases of about 1.21-folds and 1.34-folds were estimated, passing from 2.5 to 5.0 mA cm^{-2}, and from 5.0 to 15.0 mA cm^{-2}, respectively. However, there are significant differences in the persulfate concentrations electrochemically generated.

Another feature that should be indicated is that a successive intensification on the *j* could favor an increase in the production of $^{\bullet}OH$ radicals as well as an increase in the oxygen evolution reaction [43–45]. In the former, these can react with the SO_4^{2-} ions in the diffusion layer to form $SO_4^{-\bullet}$ (Eq. 3); and subsequently, produce $S_2O_8^{2-}$ [42,46]. Meanwhile, when *j* increases significantly, these can be also wasted favoring the production of O_2 (Eq. 6), in the latter. These assertions are in agreement with the behavior reported by Pires *et al.* using BDD electrode [36], by applying *j* values higher than 15 mA cm^{-2}. On the contrary, at BDD/B:CNW anode, more active BDD ($SO_4^{-\bullet}$)-sites on the diamond surface can be formed by increasing the *j* values (Eq. 3), favoring an increase in the production of persulfate via Eqs. (4) and (5).

To understand the fundamentals of the mechanism related to the nature of electrocatalytic material, the electrogeneration of persulfate at diamond electrodes was also

391 compared to TiPt, Pb/PbO_2 and Ti/TiO_2-nanotubes/PbO_2. As can be observed at Fig. 4, it is
392 evident that $S_2O_8^{2-}$ is efficiently produced at both diamond electrodes, by applying different
393 *j*, with respect to the other anodic materials. This enhancement in the persulfate
394 electrosynthesis is due to the mechanisms associated with the anodic surfaces used as well
395 as the extension of each one of them.

396 Primarily, it is important to remark that no similar production of $^{\bullet}OH$ radicals, via
397 water discharge, is attained at all electrocatalytic materials due to their active and non-active
398 nature. Then, following this statement [1,35], higher production of $^{\bullet}OH$ radicals implies
399 higher production of persulfate. For example, Ti/Pt produced lower concentrations of $S_2O_8^{2-}$
400 (0.36, 0.42 and 0.5 μM at 2.5, 5.0 and 15.0 mA cm^{-2}, respectively) because lower
401 electrogeneration of $^{\bullet}OH$ radicals was reached at its surface, limiting the electrosynthesis
402 mechanism via the participation of free heterogeneous $^{\bullet}OH$ Eqs. (3), (7) and (8).

403 Conversely, at the diamond electrode (e.g.: BDD plate), the efficient production of
404 $^{\bullet}OH$ radicals is attained, favoring the generation of $S_2O_8^{2-}$ (such as 3.65, 4.87 and 7.98 μM
405 at 2.5, 5.0 and 15.0 mA cm^{-2}, respectively) via the formation of $SO_4^{-\bullet}$.

406 $$SO_4^{-\bullet} + SO_4^{-\bullet} \rightarrow S_2O_8^{2-} \quad (8)$$

407 Secondly, the formation of $S_2O_8^{2-}$ via direct electron transfer and/or via ($SO_4^{-\bullet}$)-active
408 sites on the electrode surfaces depends on the interaction of SO_4^{2-} ions and the
409 electrocatalytic activity of each anode. In this frame, although the extension of the
410 mechanisms is not completely clear, it seems that the electrogeneration of $S_2O_8^{2-}$, via direct
411 oxidation of SO_4^{2-}, is attained at Ti/Pt surface, as the main approach, confirming that a

412 complex set of electrochemical and chemical reactions can be attained at non-active anodes
413 and consequently, improving the electrosynthesis yield of $S_2O_8^{2-}$ concentration.

414

415 **3.4. Electrochemical oxidation of a target organic compound**

416 To evaluate the performance of the persulfate electrochemically generated at diamond
417 surfaces and the other materials, oxidation in-situ experiments were carried out. Solutions of
418 25 mL of 0.05 M of Na_2SO_4 containing 10 mg L^{-1} of MO were electrochemically treated by
419 applying 15 mA cm^{-2}, mixing with magnetic stirring during 40 min and aliquots were
420 withdrawn at predetermined times to determine the color removal, COD decay, and the
421 concentration of the target pollutant by an electroanalytic procedure. As can be observed in
422 Fig. 5, EO process with BDD/B:CNW anode removed more than 95% of solution color in 5
423 min of electrolysis. Meanwhile, 93.8%, 95.7%, 98.6% and 85.8% were removed in 7, 10, 15
424 and 25 min at BDD plate, Ti/TiO_2-nanotubes/PbO_2, Pb/PbO_2 and TiPt, respectively.
425 According to the spectrophotometric measurements, the intensity of the visible band at 465
426 nm continuously diminished until it disappears as a function of time during the galvanostatic
427 electrolysis, leading to complete solution discoloration, in all cases. However, the absorbance
428 changes were reasonably rapid at BDD/B:CNW, BDD plate, Ti/TiO_2-nanotubes/PbO_2 and
429 Pb/PbO_2 anodes, indicating that the fragmentation of the MO chromophore group is rapidly
430 attained [29], promoting the elimination of color's solution and after that, the formation of
431 many other intermediates.

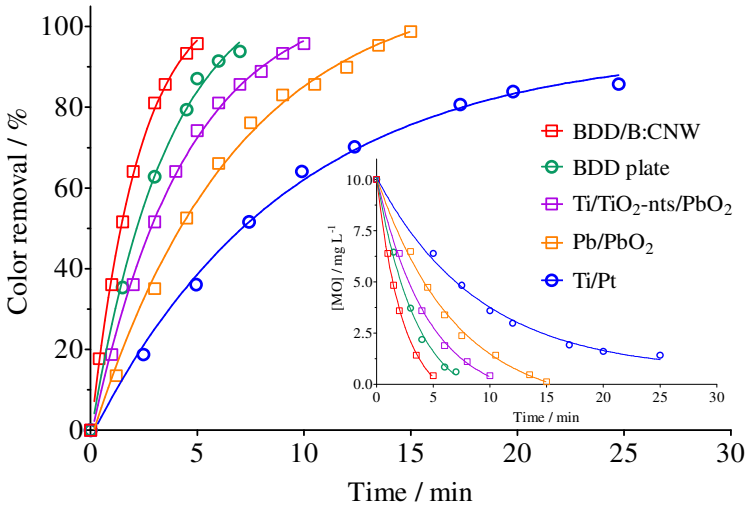

Fig. 5. Color removal effectiveness, as a function of time, at different anodic materials electrogenerating *in-situ* sulfate-based oxidizing species by applying 15 mA cm^{-2} at 25°C. Inset: MO concentration decay, as a function of time, under similar experimental conditions.

In fact, when MO concentration was followed during the EO tests, it gradually decreased and it was dependent on the nature of the material used. Again, non-active anodes were more efficient to remove MO from the solution (inset in Fig. 5), following an efficacy order as BDD/B:CNW>BDD plate>Ti/TiO_2-nanotubes/PbO_2>Pb/PbO_2>Ti/Pt. Only Ti/Pt anode was less efficient, achieving 85% of removal from the MO initial concentration. Analyzing the results obtained, BDD/B:CNW seems to be the most efficient anodic material for the elimination of organic compounds from aqueous solution via SO_4^{2-}/$SO_4^{\bullet-}$/$S_2O_8^{2-}$ system in concomitance with free heterogeneous $^{\bullet}$OH. However, the elimination of color and MO is not an indicator of the effective removal of organic matter. Therefore, COD removal was evaluated, at the end of the electrolysis time (40 min), by applying low and high *j* values

(2.5 and 15 mA cm^{-2}). As observed in Fig. 6, different residual values of COD were determined indicating that the organic matter was oxidized in all cases.

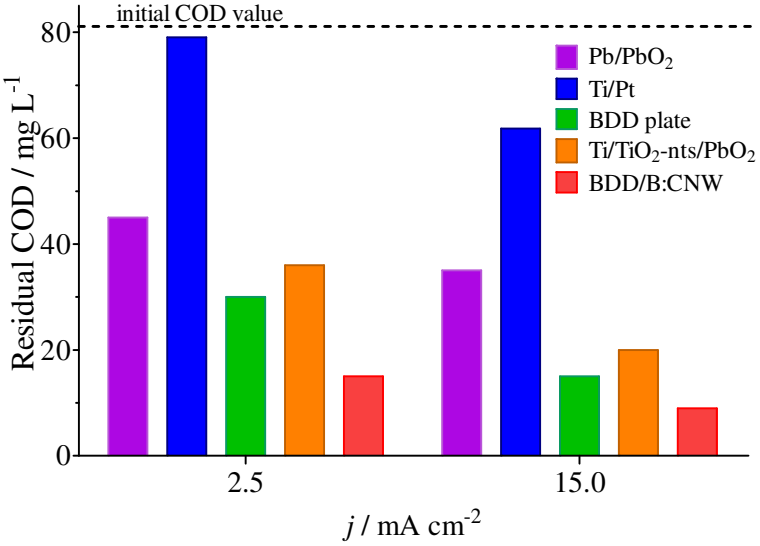

Fig. 6. Residual COD values, as a function of j (2.5 and 15.0 mA cm^{-2}), after 40 min of electrolysis at different anodic materials in EO tests at 25°C.

On the one hand, residual COD concentrations in solution of about 15.1 and 9.0 mg L^{-1} were determined at 2.5 and 15 mA cm^{-2} with BDD/B:CNW anode corresponding to 81.80% and 89.15% of COD removals, considering 83.0 mg L^{-1} as initial COD. On the other hand, lower COD removals (4.76% and 25.51% at 2.5 and 15 mA cm^{-2}, respectively) were achieved using Ti/Pt, as electrocatalytic material, that still represents a significant amount of dissolved organic matter in solution. Based on these results, it is clear that the elimination of organic matter occurred by the reactions attained in the reaction cage as surface-layer-based approaches via $SO_4^{\bullet-}$, $S_2O_8^{2-}$ and free heterogeneous $^{\bullet}OH$. But, the intensification of the

460 process is attained when a synergic effect is reached via the participation of all oxidant
461 species, which depends on the extension of the electrogeneration of each one of the oxidants,
462 mainly at non-active anodes.

463 The results obtained at diamond electrodes, such as the real surface area, Tafel plots,
464 persulfate production, and electrochemical degradation, evidenced that the concentration of
465 $SO_4^{\bullet-}$, $S_2O_8^{2-}$ and free heterogeneous $^{\bullet}OH$ could be different, under the experimental
466 conditions exposed here. This hypothesis is mainly related to the efficacy to produce
467 persulfate, discoloration level, and MO decay as well as COD removal comparing both BDD
468 plate and BDD/B:CNW anodes. In the former, all parameters were efficiently achieved and
469 superior to BDD/B:CNW anode. Meanwhile, COD was significantly removed from synthetic
470 effluent at BDD/B:CNW anode than the other electrodes. This behavior could be associated
471 with the electrochemical generation of prior species that reacts in Nernst layer with the
472 organic compound before generating $S_2O_8^{2-}$. According to the literature [8,29], $SO_4^{-\bullet}$ radicals
473 are the potential candidate, as already experimental [41] and theoretically [47] established;
474 in the case of diamond electrodes, the formation of BDD-($SO_4^{\bullet-}$) sites is a pre-requisite step
475 to produce $S_2O_8^{2-}$ by recombining two $SO_4^{\bullet-}$ species (Eq. (13)). However, as already proved
476 by electrochemical measurements, this behavior is strongly dependent on the carbon sp^2-
477 impurities content on the BDD surface. Graphitic sp^2 carbon act as the adsorption site for
478 sulfate-based species (e.g., SO_4^{2-}, HSO_4^-) at the diamond electrode, favoring the generation
479 of $SO_4^{-\bullet}$, thus producing $S_2O_8^{2-}$. In the case of BDD/B:CNW electrode, its surface was
480 meaningly enlarged due to the 3D-diamond-carbon nanostructures. These nanostructures
481 (nano-flaps, nanowalls, as well as microcavities and micro-valleys) contain a key quantity of
482 hot-spot active sites, which could participate as adsorption sulfate-based species.

3D-diamond-carbon nanostructures + $SO_4^{2-}{}_{(aq)}$ → 3D-diamond-carbon nanostructures-(SO_4^{2-})$_{ads}$ (9)

3D-diamond-carbon nanostructures-($SO_4^{-\bullet}$)$_{ads}$ + $SO_4^{-\bullet}$ → $S_2O_8^{2-}$ (10)

In this context, the formation of active-($SO_4^{-\bullet}$) sites is mainly attained at BDD/B:CNW (Eq. 9), producing higher concentrations of $SO_4^{-\bullet}$ at its surface when compared to the production of free heterogeneous $^{\bullet}$OH. Although similar oxidation-reduction potentials are registered between $SO_4^{-\bullet}$ (2.5–3.1 V vs. NHE) and $^{\bullet}$OH (2.74 V vs. NHE), different extinction lifetimes are attained in solution, 30–40 μs for $SO_4^{-\bullet}$ and less than 1 μs for $^{\bullet}$OH [8], which allows to substantially improve the $SO_4^{-\bullet}$ mass transfer performances and subsequently, its contact chance and effectiveness with the pollutants in solution, as *surface-layer-* or as *volume-solution-* oxidation approaches [3,8,9,29,48]. Additionally, a wide pH window (from 2.0 to 8.0), due to the pH adjustment, can be used to favor the efficacy of the $SO_4^{-\bullet}$ with the organic pollutants. Consequently, BDD/B:CNW produces a higher concentration of $SO_4^{-\bullet}$ that, which is available at active sites on its surface with a substantial lifetime, enhances the organic matter removal (see Fig. 6) concerning other electrodes, mainly BDD plate.

Conclusions

In summary, we can conclude that,

(i) BDD/B:CNW electrode is constituted by 3D-diamond-carbon nanostructures which increase significantly its electroactive surface area, as confirmed by the double layer capacitance determination obtaining an expansion of about 3.2-folds respect to the area of a BDD plate.

(ii) The roughness factor indicated that the 3D-nanomaterial increased its porous properties which were also confirmed by SEM images for BDD/B:CNW surface.

(iii) In both diamond materials, electrochemical measurements have indicated that the complex set of the electrochemical reactions takes at lower and higher over potential regions. However, it mainly seems that the persulfate electrosynthesis depends on the stability/reactivity of $^{\bullet}OH$ and diamond surface active sites to favor the production of $SO_4^{-\bullet}$. In the case of BDD plate, it produces rapidly $SO_4^{-\bullet}$, via reaction between $^{\bullet}OH$ and SO_4^{2-}, which form $S_2O_8^{2-}$, but it is a less reactive oxidizing species. Meanwhile, $SO_4^{-\bullet}$ species are adsorbed at sp2-active sites at BDD/B:CNW favoring their participation in the oxidation of MO.

(iv) In the case of PbO_2-based electrodes, indirect oxidation of SO_4^{2-} via heterogeneous free $^{\bullet}OH$ can be hypnotized where a possible formation of the active-($SO_4^{-\bullet}$) sites can be also feasible at α- PbO_2 or β- PbO_2 sites, which should be still completely elucidated.

These conclusions open a new landscape associated with the real mechanism to produce sulfate-based oxidizing species at BDD anodes as well as the electrochemical generation of these oxidants at other non-active and active anodes.

4. Acknowledgments

Financial supports from Conselho Nacional de Desenvolvimento Científico e Tecnológico (CNPq, Brazil) (306323/2018-4, 312595/2019-0, 439344/2018-2), and from Fundação de Amparo à Pesquisa do Estado de São Paulo (Brazil), FAPESP 2014/50945-4 and 2019/13113-4, are gratefully acknowledged. Carlos A. Martínez-Huitle acknowledges the funding provided by the Alexander von Humboldt Foundation (Germany) and CAPES (Brazil) as a Humboldt fellowship for Experienced Researcher (88881.136108/2017-01) at the Johannes Gutenberg-Universität Mainz, Germany. Robert Bogdanowicz acknowledges funding by the National Center for Research and Development through the Project NOR/POLNOR/i-CLARE/0038/2019.

5. References

[1] C.A. Martínez-Huitle, M. Panizza, Electrochemical oxidation of organic pollutants for wastewater treatment, Curr. Opin. Electrochem. 11 (2018) 62–71. https://doi.org/10.1016/j.coelec.2018.07.010.

[2] C.A. Martínez-Huitle, M.A. Rodrigo, I. Sirés, O. Scialdone, C.A. Martinez-Huitle, M.A. Rodrigo, I. Sire, O. Scialdone, Single and Coupled Electrochemical Processes and Reactors for the Abatement of Organic Water Pollutants: A Critical Review, Chem. Rev. 115 (2015) 13362–13407. https://doi.org/10.1021/acs.chemrev.5b00361.

[3] S.O. Ganiyu, C.A. Martínez-Huitle, M.A. Oturan, Electrochemical advanced oxidation processes for wastewater treatment: Advances in formation and detection of reactive species and mechanisms, Curr. Opin. Electrochem. 27 (2021). https://doi.org/10.1016/j.coelec.2020.100678.

[4] S.O. Ganiyu, E.V. dos Santos, C.A. Martínez-Huitle, S.R. Waldvogel, Opportunities

and challenges of thin-film boron-doped diamond electrochemistry for valuable resources recovery from waste: Organic, inorganic, and volatile product electrosynthesis, Curr. Opin. Electrochem. (2021) 100903. https://doi.org/10.1016/J.COELEC.2021.100903.

[5] G.R. Salazar-Banda, G.D.O.S. Santos, I.M. Duarte Gonzaga, A.R. Dória, K.I. Barrios Eguiluz, Developments in electrode materials for wastewater treatment, Curr. Opin. Electrochem. 26 (2021). https://doi.org/10.1016/j.coelec.2020.100663.

[6] D. Clematis, M. Panizza, Application of boron-doped diamond electrodes for electrochemical oxidation of real wastewaters, Curr. Opin. Electrochem. (2021) 100844. https://doi.org/10.1016/J.COELEC.2021.100844.

[7] P.V. Nidheesh, M. Zhou, M.A. Oturan, An overview on the removal of synthetic dyes from water by electrochemical advanced oxidation processes, Chemosphere. 197 (2018) 210–227. https://doi.org/10.1016/j.chemosphere.2017.12.195.

[8] G. Divyapriya, P. V. Nidheesh, Electrochemically generated sulfate radicals by boron doped diamond and its environmental applications, Curr. Opin. Solid State Mater. Sci. 25 (2021) 100921. https://doi.org/10.1016/J.COSSMS.2021.100921.

[9] C.A. Martínez-Huitle, E. Brillas, A critical review over the electrochemical disinfection of bacteria in synthetic and real wastewaters using a boron-doped diamond anode, Curr. Opin. Solid State Mater. Sci. 25 (2021) 100926. https://doi.org/10.1016/j.cossms.2021.100926.

[10] K. Groenen Serrano, A critical review on the electrochemical production and use of peroxo-compounds, Curr. Opin. Electrochem. 27 (2021) 100679. https://doi.org/10.1016/j.coelec.2020.100679.

[11] A.S. Mora, S.T. McBeath, C.A. Cid, M.R. Hoffmann, N.J.D. Graham, Diamond

electrode facilitated electrosynthesis of water and wastewater treatment oxidants, Curr. Opin. Electrochem. 32 (2022) 100899. https://doi.org/10.1016/J.COELEC.2021.100899.

[12] G.R. Pointer Malpass, A. de Jesus Motheo, Recent advances on the use of active anodes in environmental electrochemistry, Curr. Opin. Electrochem. (2021) 100689. https://doi.org/10.1016/j.coelec.2021.100689.

[13] X. Du, M.A. Oturan, M. Zhou, N. Belkessa, P. Su, J. Cai, C. Trellu, E. Mousset, Nanostructured electrodes for electrocatalytic advanced oxidation processes: From materials preparation to mechanisms understanding and wastewater treatment applications, Appl. Catal. B Environ. 296 (2021) 120332. https://doi.org/10.1016/J.APCATB.2021.120332.

[14] M. Pierpaoli, P. Jakobczyk, M. Sawczak, A. Łuczkiewicz, S. Fudala-Książek, R. Bogdanowicz, Carbon nanoarchitectures as high-performance electrodes for the electrochemical oxidation of landfill leachate, J. Hazard. Mater. 401 (2021) 123407. https://doi.org/10.1016/J.JHAZMAT.2020.123407.

[15] M. Pierpaoli, M. Szopińska, B.K. Wilk, M. Sobaszek, A. Łuczkiewicz, R. Bogdanowicz, S. Fudala-Książek, Electrochemical oxidation of PFOA and PFOS in landfill leachates at low and highly boron-doped diamond electrodes, J. Hazard. Mater. 403 (2021). https://doi.org/10.1016/j.jhazmat.2020.123606.

[16] S. Dutta, A. Bhaumik, K.C.W. Wu, Hierarchically porous carbon derived from polymers and biomass: effect of interconnected pores on energy applications, Energy Environ. Sci. 7 (2014) 3574–3592. https://doi.org/10.1039/C4EE01075B.

[17] B.K. Mishra, S. Chakraborty, P. Kumar, C. Saraswat, Sustainable Solutions for Urban Water Security, 93 (2020). https://doi.org/10.1007/978-3-030-53110-2.

600 [18] B. Van der Bruggen, Sustainable implementation of innovative technologies for
601 water purification, Nat. Rev. Chem. 2021 54. 5 (2021) 217–218.
602 https://doi.org/10.1038/s41570-021-00264-7.
603 [19] M. Pierpaoli, A. Dettlaff, M. Szopińska, K. Karpienko, M. Wróbel, A. Łuczkiewicz,
604 S. Fudala-Książek, R. Bogdanowicz, Simultaneous opto-electrochemical monitoring
605 of carbamazepine and its electro-oxidation by-products in wastewater, J. Hazard.
606 Mater. 419 (2021). https://doi.org/10.1016/j.jhazmat.2021.126509.
607 [20] R. Bogdanowicz, Functionalized nanodiamonds as a perspective green carbo-catalyst
608 for removal of emerging organic pollutants, Curr. Opin. Solid State Mater. Sci. 26
609 (2022) 100991. https://doi.org/10.1016/J.COSSMS.2022.100991.
610 [21] R. Bogdanowicz, J. Ryl, Structural and electrochemical heterogeneities of boron-
611 doped diamond surfaces, Curr. Opin. Electrochem. 31 (2022) 100876.
612 https://doi.org/10.1016/J.COELEC.2021.100876.
613 [22] K. Siuzdak, M. Ficek, M. Sobaszek, J. Ryl, M. Gnyba, P. Niedziałkowski, N.
614 Malinowska, J. Karczewski, R. Bogdanowicz, Boron-Enhanced Growth of Micron-
615 Scale Carbon-Based Nanowalls: A Route toward High Rates of Electrochemical
616 Biosensing, ACS Appl. Mater. Interfaces. 9 (2017) 12982–12992.
617 https://doi.org/10.1021/ACSAMI.6B16860/SUPPL_FILE/AM6B16860_SI_001.PD
618 F.
619 [23] A. Dettlaff, P. Jakóbczyk, M. Ficek, B. Wilk, M. Szala, J. Wojtas, T. Ossowski, R.
620 Bogdanowicz, Electrochemical determination of nitroaromatic explosives at boron-
621 doped diamond/graphene nanowall electrodes: 2,4,6-trinitrotoluene and 2,4,6-
622 trinitroanisole in liquid effluents, J. Hazard. Mater. 387 (2020) 121672.
623 https://doi.org/10.1016/J.JHAZMAT.2019.121672.

624 [24] M. Sobaszek, K. Siuzdak, J. Ryl, M. Sawczak, S. Gupta, S.B. Carrizosa, M. Ficek,
625 B. Dec, K. Darowicki, R. Bogdanowicz, Diamond Phase (sp3-C) Rich Boron-Doped
626 Carbon Nanowalls (sp2-C): Physicochemical and Electrochemical Properties, J.
627 Phys. Chem. C. 121 (2017) 20821–20833.
628 https://doi.org/10.1021/ACS.JPCC.7B06365/ASSET/IMAGES/MEDIUM/JP-2017-
629 063658_0016.GIF.
630 [25] S. Trasatti, Electrocatalysis: understanding the success of DSA®, Electrochim. Acta.
631 45 (2000) 2377–2385. https://doi.org/10.1016/S0013-4686(00)00338-8.
632 [26] C. Calas-Blanchard, M. Comtat, J.L. Marty, S. Mauran, Textural characterisation of
633 graphite matrices using electrochemical methods, Carbon N. Y. 41 (2003) 123–130.
634 https://doi.org/10.1016/S0008-6223(02)00269-5.
635 [27] M. Łukaszewski, Electrochemical Methods of Real Surface Area Determination of
636 Noble Metal Electrodes – an Overview, Int. J. Electrochem. Sci. 11 (2016) 4442–
637 4469. https://doi.org/10.20964/2016.06.71.
638 [28] C. Liang, C.F. Huang, N. Mohanty, R.M. Kurakalva, A rapid spectrophotometric
639 determination of persulfate anion in ISCO, Chemosphere. 73 (2008) 1540–1543.
640 https://doi.org/10.1016/j.chemosphere.2008.08.043.
641 [29] K.C.F. Araújo, K.N.O. Silva, M.K.S. Monteiro, D.R. da Silva, M.A. Quiroz, E.V.
642 dos Santos, C.A. Martínez-Huitle, Towards Use of Persulfate Electrogenerated at
643 Boron Doped Diamond Electrodes as Ex-Situ Oxidation Approach: Storage and
644 Service-Life Solution Parameters, J. Electrochem. Soc. 169 (2022) 033506.
645 https://doi.org/10.1149/1945-7111/AC59F8.
646 [30] G.O.S. Santos, K.I.B. Eguiluz, G.R. Salazar-Banda, C. Sáez, M.A. Rodrigo,
647 Understanding the electrolytic generation of sulfate and chlorine oxidative species

with different boron-doped diamond anodes, J. Electroanal. Chem. 857 (2020) 113756. https://doi.org/10.1016/j.jelechem.2019.113756.

[31] H. Huang, M. Yan, C. Yang, H. He, Q. Jiang, L. Yang, Z. Lu, Z. Sun, X. Xu, Y. Bando, Y. Yamauchi, Graphene Nanoarchitectonics: Recent Advances in Graphene-Based Electrocatalysts for Hydrogen Evolution Reaction, Adv. Mater. 31 (2019) 1903415. https://doi.org/10.1002/ADMA.201903415.

[32] O.A. Trasatti, S, Petri, Real surface area measurements in electrochemistry, J. Electroanal. Chem. 327 (1992) 353–376. https://doi.org/https://doi.org/10.1016/0022-0728(92)80162-W.

[33] J.M. Doña Rodríguez, J.A. Herrera Melián, J. Pérez Peña, Determination of the Real Surface Area of Pt Electrodes by Hydrogen Adsorption Using Cyclic Voltammetry, J. Chem. Educ. 77 (2000) 1195. https://doi.org/10.1021/ed077p1195.

[34] R. Bogdanowicz, A. Fabiańska, L. Golunski, M. Sobaszek, M. Gnyba, J. Ryl, K. Darowicki, T. Ossowski, S.D. Janssens, K. Haenen, E.M. Siedlecka, Influence of the boron doping level on the electrochemical oxidation of the azo dyes at Si/BDD thin film electrodes, Diam. Relat. Mater. 39 (2013) 82–88. https://doi.org/https://doi.org/10.1016/j.diamond.2013.08.004.

[35] J. Ryl, L. Burczyk, A. Zielinski, M. Ficek, A. Franczak, R. Bogdanowicz, K. Darowicki, Heterogeneous oxidation of highly boron-doped diamond electrodes and its influence on the surface distribution of electrochemical activity, Electrochim. Acta. 297 (2019) 1018–1027. https://doi.org/10.1016/J.ELECTACTA.2018.12.050.

[36] J.P. De Paiva Barreto, K.C. De Freitas Aráujo, D.M. De Aráujo, C.A. Martínez-Huitle, Effect of sp3/sp2 ratio on boron doped diamond films for producing persulfate, ECS Electrochem. Lett. 4 (2015) E9–E11.

https://doi.org/10.1149/2.0061512eel.

[37] T.F. Da Costa, J.E.L. Santos, D.R. da Silva, C.A. Martinez-Huitle, BDD-electrolysis of oxalic acid in diluted acidic solutions, J. Braz. Chem. Soc. 30 (2019) 1541–1547. https://doi.org/10.21577/0103-5053.20190051.

[38] P.K. Jiwanti, K. Natsui, K. Nakata, Y. Einaga, The electrochemical production of C2/C3 species from carbon dioxide on copper-modified boron-doped diamond electrodes, Electrochim. Acta. 266 (2018) 414–419. https://doi.org/10.1016/j.electacta.2018.02.041.

[39] P.A. Michaud, M. Panizza, L. Ouattara, T. Diaco, G. Foti, C. Comninellis, Electrochemical oxidation of water on synthetic boron-doped diamond thin film anodes, J. Appl. Electrochem. 33 (2003) 151–154. https://doi.org/10.1023/A:1024084924058.

[40] K. Serrano, P.A. Michaud, C. Comninellis, A. Savall, Electrochemical preparation of peroxodisulfuric acid using boron doped diamond thin film electrodes, Electrochim. Acta. 48 (2002) 431–436. https://doi.org/https://doi.org/10.1016/S0013-4686(02)00688-6.

[41] K.C. de Freitas Araújo, D.R. da Silva, E.V. dos Santos, H. Varela, C.A. Martínez-Huitle, Investigation of persulfate production on BDD anode by understanding the impact of water concentration, J. Electroanal. Chem. 860 (2020) 113927. https://doi.org/10.1016/j.jelechem.2020.113927.

[42] Y.U. Shin, H.Y. Yoo, Y.Y. Ahn, M.S. Kim, K. Lee, S. Yu, C. Lee, K. Cho, H. il Kim, J. Lee, Electrochemical oxidation of organics in sulfate solutions on boron-doped diamond electrode: Multiple pathways for sulfate radical generation, Appl. Catal. B Environ. 254 (2019) 156–165.

https://doi.org/10.1016/J.APCATB.2019.04.060.

[43] W. Wu, Z.H. Huang, T.T. Lim, Recent development of mixed metal oxide anodes for electrochemical oxidation of organic pollutants in water, Appl. Catal. A Gen. 480 (2014) 58–78. https://doi.org/10.1016/J.APCATA.2014.04.035.

[44] M.S.M. Sillanpää, Electrode materials used for electrochemical oxidation of organic compounds in wastewater, (n.d.). https://doi.org/10.1007/s11157-017-9426-1.

[45] M. Moradi, Y. Vasseghian, A. Khataee, M. Kobya, H. Arabzade, E.N. Dragoi, Service life and stability of electrodes applied in electrochemical advanced oxidation processes: A comprehensive review, J. Ind. Eng. Chem. 87 (2020) 18–39. https://doi.org/10.1016/J.JIEC.2020.03.038.

[46] L.W. Matzek, M.J. Tipton, A.T. Farmer, A.D. Steen, K.E. Carter, Understanding Electrochemically Activated Persulfate and Its Application to Ciprofloxacin Abatement, Environ. Sci. Technol. 52 (2018) 5875–5883. https://doi.org/10.1021/ACS.EST.8B00015/SUPPL_FILE/ES8B00015_SI_001.PDF.

[47] J. Davis, J.C. Baygents, J. Farrell, Understanding Persulfate Production at Boron Doped Diamond Film Anodes, Electrochim. Acta. 150 (2014) 68–74. https://doi.org/10.1016/j.electacta.2014.10.104.

[48] K.N.O. Silva, K.C.F. Araújo, D.R. da Silva, C.A. Martínez-Huitle, E.V. dos Santos, Persulfate-soil washing: The green use of persulfate electrochemically generated with diamond electrodes for depolluting soils, J. Electroanal. Chem. 895 (2021) 115498. https://doi.org/10.1016/j.jelechem.2021.115498.